MAGNETIC RESONANCE
Open Access
Discussions

1 # Performance of cross-polarization experiment at conditions of
2 radiofrequency field inhomogeneity and slow to ultrafast MAS

3

4 **Andrej Šmelko[1], Jan Blahut[2], Bernd Reif[3,4,*], Zdeněk Tošner[1,*]**

5

6 [1]Department of Chemistry, Faculty of Science, Charles University, Albertov 6, 12842 Prague, Czech
7 Republic

8 [2]Institute of Organic Chemistry and Biochemistry of the CAS, Flemingovo nám. 2, 16610, Prague, Czech
9 Republic

10 [3]Bayerisches NMR Zentrum (BNMRZ) at School of Natural Sciences, Department of Bioscience,
11 Technische Universität München (TUM), Lichtenbergstr. 4, 85747 Garching, Germany

12 [4]Helmholtz-Zentrum München (HMGU), Deutsches Forschungszentrum für Gesundheit und Umwelt,
13 85764 Neuherberg, Germany

14

15 *Corresponding authors:

16 • Zdeněk Tošner, zdenek.tosner@natur.cuni.cz
17 • Bernd Reif, reif@tum.de

18

19

20 ## Abstract

21 In this manuscript, we provide an analytical description of the performance of the cross-polarization
22 experiment, including linear ramp and adiabatic tangential sweep modifications, using effective
23 Hamiltonians and simple rotations in 3D space. It is shown that radiofrequency field inhomogeneity
24 induces a reduction of the transfer efficiency at increasing MAS frequencies for both the ramp and the
25 adiabatic CP experiments. The effect depends on the ratio of the dipolar coupling constant and the
26 sample rotation frequency. In particular, our simulations show that for small dipolar couplings (1 kHz)
27 and ultrafast MAS (above 100 kHz) the transfer efficiency is below 40% when extended contact times
28 up to 20 ms are used and relaxation losses are ignored. New recoupling and magnetization transfer
29 techniques that are designed explicitly to account for inhomogeneous RF fields are needed.

30

31

MAGNETIC RESONANCE
Open Access
Discussions

1. Introduction

Cross polarization is a remarkable experiment with a very long history (Schaefer, 2007). In 1962, Hartmann and Hahn (Hartmann and Hahn, 1962) presented the theory of magnetization transfer in a two-spin system under conditions of double radiofrequency irradiation of a static sample. In 1973, Pines et al. (Pines et al., 1973) published their seminal work on proton-enhanced solid-state NMR of dilute spins such as ^{13}C and ^{15}N. While magic angle spinning (MAS) was introduced by Andrew et al. (ANDREW et al., 1958) and independently by Lowe (Lowe, 1959) already in 1958 and 1959, respectively, it was only in 1977 that cross polarization was successfully combined with sample rotation. The necessary modification of the Hartmann-Hahn conditions was described by Stejskal et al. (Stejskal et al., 1977). After that, many modifications with variable amplitude irradiations on one or both rf channels were developed. Among them, simple linear ramps (Metz et al., 1994) and adiabatic sweeps (Hediger et al., 1995) became most popular. Ramp-CP was originally introduced to broaden the Hartmann-Hahn (HH) matching condition and to obtain uniform signal amplitudes. In the original publication, low MAS frequencies (below ~10 kHz) were used and the sweep could cover several HH conditions. At the same time, it was realized that the largest enhancement in signal intensity is obtained when the sweep covers only one HH condition (Metz et al., 1994). The RF amplitude sweep implies a partially adiabatic inversion of the spins and compensates RF field inhomogeneities (Peersen et al., 1994; Hediger et al., 1995).

Until now, cross-polarization remains the main pulse sequence building block for magnetization transfers. At very high MAS frequencies, it becomes difficult to achieve HH zero-quantum matching where the difference of the two applied rf amplitudes is equal to the MAS frequency. Instead, the HH double-quantum matching condition must be used in which the sum of the RF amplitudes equals the MAS frequency. The spin dynamics remains the same with the exception that negative intensities are obtained. Cross-polarization is thus applied over an exceptionally wide range of conditions, from experiments using static samples to MAS experiments with rotation frequencies above 100 kHz.

Developments in NMR hardware and pulse sequences are largely driven by biomolecular applications. Due to difficulties in sample preparation, only limited amounts of material are available that do not allow to completely fill the MAS rotor. It has been noticed that restriction of the sample volume to 30% with aligning the sample in the center of the solenoidal coil does not lead to a substantial reduction in sensitivity in $^{15}N,^{13}C$ correlation experiments. This volume-selective behavior of the cross-polarization experiment is due to the inhomogeneous radiofrequency (RF) field distribution generated by the solenoidal coil. Although the RF field is rather homogeneous in the central area of the rotor, it quickly decays towards the end of the coil and cross-polarization mediated polarization transfer is impaired due to mismatch of RF amplitudes. The limited availability of biological sample and the use of center-packed rotors are presumably the reason why the detrimental effects of RF field inhomogeneity were neglected in the development of new solid-state NMR experiments for so long. The rotors for ultrafast MAS, however, are small and can be completely filled with sample. Under these conditions, RF inhomogeneity comes up as a concern. With faster MAS and correspondingly smaller rotors that contain less material, we are facing again sensitivity issues. It is obviously desirable that the whole sample contributes to the NMR signal. At this point, it appears that the inhomogeneity of the RF field is the prevailing challenge for the development of new solid-state NMR methods.

73   In this tutorial article, we summarize the principles of the cross polarization (CP) experiment and focus
74   on the effect of RF field inhomogeneity. For demonstration purposes we limit our treatment to an
75   isolated heteronuclear pair of spin-1/2 nuclei that are coupled via the dipole-dipole interaction. We
76   assume that there is no chemical shift interaction. Using average Hamiltonian theory and simple 3D
77   rotations we explain the process of magnetization transfer assuming different amplitude swept CP
78   variants. We show that the total signal measured after the CP transfer decreases with increasing MAS
79   frequency. The effect is amplified for small dipolar couplings. We numerically optimize linear ramp and
80   adiabatic tangential sweep experiments to identify the conditions for the best performance as a
81   function of the dipolar coupling constant, contact time, and MAS frequency. Neither of these
82   techniques under any condition fully compensates for RF field inhomogeneities. The most striking
83   example of low efficiency is the CP transfer between a ^{15}N nucleus directly bonded to a ^{13}C atom
84   involving a dipolar coupling constant of about 1 kHz. With the forthcoming MAS technology in mind
85   that can reach MAS frequencies of up to 200 kHz, we predict that only 20% of the sample will
86   contribute to the NMR signal after a CP mixing time of 10 ms. It clearly calls for the development of
87   alternative magnetization transfer techniques that are suitable for ultrafast MAS NMR experiments.

88

89   ## 2. Theory

90   A theoretical description of the cross polarization phenomenon can be found in many solid-state NMR
91   textbooks. Here, we revisit the relevant parts and focus on visualization of the magnetization transfer
92   process during variable-amplitude sequences, following the description presented by Rovnyak
93   (Rovnyak, 2008). In the following, we assume an isolated spin pair. A more general description that
94   considers the surrounding spins can be found, for example, in the work of Vega et al. (Ray et al., 1998)

95   ### 2.1. Hamiltonian decomposition into ZQ and DQ subspaces

96   We start with the Hamiltonian that contains the dipole-dipole interaction and the radiofrequency fields
97   with amplitudes ω_I and ω_S applied on resonance to spins I and S, respectively.

$$H = \omega_I I_x + \omega_S S_x + d_{IS}(t) 2 I_z S_z \tag{1}$$

98   The dipolar term is time dependent due to magic angle spinning (angular frequency ω_R) and can be
99   expressed as

$$d_{IS}(t) = g_1 \cos(\omega_R t + \gamma) + g_2 \cos(2\omega_R t + 2\gamma) \tag{2}$$

$$g_1 = -\frac{1}{\sqrt{2}} 2\pi b_{IS} \sin 2\beta \tag{3}$$

$$g_2 = \frac{1}{2} 2\pi b_{IS} \sin^2 \beta \tag{4}$$

100   where b_{IS} is the dipolar coupling constant ($b_{IS} = -\frac{\mu}{4\pi} \frac{\gamma_I \gamma_S}{r_{IS}^3}$) in units of Hertz, and β, γ are the Euler
101   angles relating the orientation of the dipolar vector $\vec{r}_{IS}$ with the rotor axis (the α angle is irrelevant as
102   the dipolar coupling tensor has a vanishing asymmetry).

103 Subsequently, the reference frame is transformed into the tilted frame where the radiofrequency
104 fields are linear with I_z and S_z, while the dipolar term becomes transversal. This transformation is
105 represented by a $\pi/2$-rotation around $(I_y + S_y)$ and we obtain

$$H' = \omega_I I_z + \omega_S S_z + d_{IS}(t) 2 I_x S_x \tag{5}$$

106 This form of the Hamiltonian allows decomposition of the spin dynamics problem into two separate
107 subspaces, the zero quantum (ZQ) and the double quantum (DQ) subspace. The ZQ and DQ subspaces
108 can be represented using fictitious spin-1/2 operators that are defined in Table 1.

109

110 **Table 1.** Fictitious spin-1/2 operators in zero quantum and double quantum subspaces.

Zero quantum	Double quantum
$I_x^{ZQ} = I_x S_x + I_y S_y$ $I_y^{ZQ} = I_y S_x - I_x S_y$ $I_z^{ZQ} = \frac{1}{2}(I_z - S_z)$	$I_x^{DQ} = I_x S_x - I_y S_y$ $I_y^{DQ} = I_y S_x + I_x S_y$ $I_z^{DQ} = \frac{1}{2}(I_z + S_z)$
Inverted relations	
$I_z = I_z^{DQ} + I_z^{ZQ}$ $\qquad S_z = I_z^{DQ} - I_z^{ZQ}$ $\qquad 2 I_x S_x = I_x^{DQ} + I_x^{ZQ}$	

111

112 The Hamiltonian can then be written as

$$H' = H^{ZQ} + H^{DQ} \tag{6}$$

$$H^{ZQ} = (\omega_I - \omega_S) I_z^{ZQ} + d_{IS}(t) I_x^{ZQ} \tag{7}$$

$$H^{DQ} = (\omega_I + \omega_S) I_z^{DQ} + d_{IS}(t) I_x^{DQ} \tag{8}$$

113

114 ### 2.2. Magnetization transfer in static CP experiment

115 The magnetization transfer process in the tilted frame is described by a transition from I_z into S_z. The
116 action of RF pulses and the dipolar interaction on the spin state I_z in the tilted frame is evaluated
117 independently in the ZQ and DQ subspace, working with the initial spin states I_z^{ZQ} and I_z^{DQ},
118 respectively. If the sample is static, the zero-quantum Hartmann-Hahn condition is $\omega_I - \omega_S = 0$ and
119 the Hamiltonian in Eq. (7) reduces to $H^{ZQ} = d_{IS} I_x^{ZQ}$ (d_{IS} is time independent). The spin state
120 represented by the operator I_z^{ZQ} is rotated around the I_x^{ZQ} axis as a consequence of the dipolar
121 interaction. Simultaneously, the spin state I_z^{DQ} evolves in the DQ subspace. We can assume that $\omega_I +$
122 ω_S is much larger than d_{IS}. The effective rotation axis is thus oriented along I_z^{DQ}, see Eq. (8). As a result,
123 H^{DQ} has no effect on the I_z^{DQ} state. This is summarized in the following equations.

$$I_z^{ZQ} \xrightarrow{H^{ZQ}} I_z^{ZQ} \cos d_{IS}t - I_y^{ZQ} \sin d_{IS}t$$

$$= \frac{1}{2}(I_z - S_z)\cos d_{IS}t - \left(I_y S_x - I_x S_y\right)\sin d_{IS}t \tag{9}$$

$$I_z^{DQ} \xrightarrow{H^{DQ}} I_z^{DQ} = \frac{1}{2}(I_z + S_z) \tag{10}$$

$$I_z = I_z^{ZQ} + I_z^{DQ} \xrightarrow{H^{ZQ}+H^{DQ}} I_z\frac{1}{2}(\cos d_{IS}t + 1) + S_z\frac{1}{2}(1 - \cos d_{IS}t)$$

$$- \left(I_y S_x - I_x S_y\right)\sin d_{IS}t \tag{11}$$

124

125 The I_z spin state is transformed into S_z when $\cos d_{IS}t = -1$, resulting in a full inversion of the I_z^{ZQ}
126 operator.

127 For the double-quantum Hartmann-Hahn condition $\omega_I + \omega_S = 0$, the rotation occurs in the DQ
128 subspace. In analogy to the previous case, we assume $|\omega_I - \omega_S| \gg d_{IS}$. Under this precondition, the
129 ZQ spin state is not changed.

$$I_z^{ZQ} \xrightarrow{H^{ZQ}} I_z^{ZQ} = \frac{1}{2}(I_z - S_z) \tag{12}$$

$$I_z^{DQ} \xrightarrow{H^{DQ}} I_z^{DQ} \cos d_{IS}t - I_y^{DQ} \sin d_{IS}t$$

$$= \frac{1}{2}(I_z + S_z)\cos d_{IS}t - \left(I_y S_x + I_x S_y\right)\sin d_{IS}t \tag{13}$$

$$I_z = I_z^{ZQ} + I_z^{DQ} \xrightarrow{H^{ZQ}+H^{DQ}} I_z\frac{1}{2}(\cos d_{IS}t + 1) - S_z\frac{1}{2}(1 - \cos d_{IS}t)$$

$$- \left(I_y S_x + I_x S_y\right)\sin d_{IS}t \tag{14}$$

130 For $\cos d_{IS}t = -1$, the I_z^{DQ} operator is inverted resulting in generation of the operator $-S_z$. Note that
131 the double quantum Hartmann-Hahn condition yields negative signal intensity.

132 The dipolar coupling is an orientation dependent interaction. The above derived results describe the
133 matching conditions for a particular crystallite orientation. To yield the magnetization transfer
134 dynamics for a powder sample, the ensemble of all possible crystallite orientations has to be accounted
135 for.

2.3. Magic angle spinning and average Hamiltonians

137 In case of MAS, the Hamiltonians become time dependent. The analysis is performed then using
138 average Hamiltonian theory (AHT) employing the Magnus expansion. A tutorial on AHT principles was
139 presented by Brinkmann (Brinkmann, 2016). To retain fast convergence of the Magnus series, the
140 Hamiltonian is expressed in an appropriate interaction frame. Eq. (2) implies four resonance conditions
141 upon transformation into a new rotating frame in which the periodic modulations of $d_{IS}(t)$ are
142 removed by application of RF fields. These resonance conditions are associated with the characteristic
143 frequencies $n\omega_R$ with $n = \pm 1, \pm 2$. We choose $n = +1$ and focus on the ZQ subspace. In general,
144 transformation to a new reference frame is described using a propagator $U_T(t)$. This propagator
145 transforms the Hamiltonian according to

$$H' = U_T^+(t)HU_T(t) - iU_T^+(t)\frac{d}{dt}U_T(t) \tag{15}$$

146   In this case, $U_T(t) = \exp\left(-i\omega_R t I_z^{ZQ}\right)$. The transformation can be regarded as a rotation around I_z^{ZQ}
147   with a frequency $-\omega_R$. The second term in Eq. (15) is a Coriolis term which introduces the term
148   $-\omega_R I_z^{ZQ}$ into the transformed Hamiltonian.

$$H^{ZQ\prime} = (\omega_I - \omega_S - \omega_R)I_z^{ZQ} + d_{IS}(t)\left(I_x^{ZQ}\cos\omega_R t - I_y^{ZQ}\sin\omega_R t\right) \tag{16}$$

149   The first order Hamiltonian is the time average over the modulation period $\tau_R = 2\pi/\omega_R$,

$$\overline{H}^{ZQ} = \frac{1}{\tau_R}\int_0^{\tau_R} H^{ZQ\prime}dt \tag{17}$$

150   The integral over the time dependent parts in Eq. (16) is evaluated as follows (making use of
151   goniometric identities)

152   $$\frac{1}{\tau_R}\int_0^{\tau_R}[g_1\cos(\omega_R t + \gamma) + g_2\cos(2\omega_R t + 2\gamma)]\left(I_x^{ZQ}\cos\omega_R t - I_y^{ZQ}\sin\omega_R t\right)dt =$$

153   $$= \frac{1}{\tau_R}\int_0^{\tau_r}\left\{g_1\frac{1}{2}[\cos(2\omega_R t + \gamma) + \cos\gamma] + g_2\frac{1}{2}[\cos(3\omega_R t + 2\gamma) + \cos(\omega_R t + 2\gamma)]\right\}dt\, I_x^{ZQ} +$$

154   $$- \frac{1}{\tau_R}\int_0^{\tau_r}\left\{g_1\frac{1}{2}[\sin(2\omega_R t + \gamma) - \sin\gamma] + g_2\frac{1}{2}[\sin(3\omega_R t + 2\gamma) - \sin(\omega_R t + 2\gamma)]\right\}dt\, I_y^{ZQ} =$$

155   $$= \frac{1}{2}g_1\cos\gamma\, I_x^{ZQ} + \frac{1}{2}g_1\sin\gamma\, I_y^{ZQ}$$

156   We obtain the first order average Hamiltonian in the ZQ subspace thus as

$$\overline{H}^{ZQ} = (\omega_I - \omega_S - \omega_R)I_z^{ZQ} + \frac{1}{2}g_1\left(\cos\gamma\, I_x^{ZQ} + \sin\gamma\, I_y^{ZQ}\right) \tag{18}$$

157   The Hartmann-Hahn condition is corrected to account for the rotation of the sample and has the form
158   $\omega_I - \omega_S = \omega_R$. In this case, the component of $\overline{H}^{ZQ}$ along the I_z^{ZQ} axis is zero and the dipolar
159   interaction results in a rotation around an axis in the transversal plane, with a phase depending on γ.
160   For each crystallite, the spin state I_z^{ZQ} is flipped away from the z axis generating a transversal
161   component. These transversal components are equally distributed with respect to the γ angle and
162   average to zero in a powder sample. Only the projection on the I_z^{ZQ} axis is relevant, and we can
163   therefore arbitrarily set $\gamma = 0$.

164   The calculation can be repeated for other choices of n and the following zero-quantum average
165   Hamiltonians are obtained

$$\overline{H}^{ZQ} = (\omega_I - \omega_S - n\omega_R)I_z^{ZQ} + \frac{1}{2}g_n I_x^{ZQ} \tag{19}$$

166 The fast convergence of the Magnus expansion is maintained and the proper description of spin
167 dynamics by an average Hamiltonian is valid in the vicinity of the Hartmann-Hahn condition ($\omega_I - \omega_S - n\omega_R = 0$).
168 $n\omega_R = 0$). The RF amplitudes ω_I and ω_S may become time dependent in case a linear ramp or an
169 adiabatic sweep is applied. In any case, we assume that RF changes are slow compared to the MAS
170 frequency to ensure validity of this treatment.

171 The analysis is completed by inspecting the spin dynamics in the DQ subspace. We apply the same
172 procedure as for the ZQ subspace, yielding

$$\bar{H}^{DQ} = (\omega_I + \omega_S - n\omega_R)I_z^{DQ} + \frac{1}{2}g_n I_x^{DQ} \tag{20}$$

173 For the zero quantum condition, it is assumed that the I_z^{DQ} term dominates the average Hamiltonian
174 $\bar{H}^{DQ}$, i.e. $\omega_I + \omega_S - n\omega_R \gg d_{IS}$ for all $n = \pm1, \pm2$. Under these conditions, the initial state I_z^{DQ}
175 remains unchanged. However, these conditions might be violated for large RF amplitude sweeps or in
176 case of substantial RF field inhomogeneity.

177 ### *2.4. CP matching profiles*

178 For constant RF amplitudes, the magnetization transfer process can be analytically described to derive
179 the so-called CP matching profiles (sometimes dubbed Hartmann-Hahn fingers). This derivation was
180 previously published by Levitt (Levitt, 1991), and Wu and Zilm (Wu and Zilm, 1993). It is assumed that
181 both the ZQ and DQ Hartmann-Hahn conditions are independent. We reiterate the calculation for the
182 matching condition and focus first on the ZQ Hamiltonian given in Eq. (19). We proceed with the final
183 transformation into the effective field of the Hamiltonian. The Hamiltonian $\bar{H}^{ZQ}$ can be represented
184 as a vector in the xz plane. This vector has an angle ϕ with the x axis. The transformation into the
185 effective field is described by a rotation around I_y^{ZQ} by an angle $-\phi$, which is equivalent to the
186 application of the propagator $U_T = \exp(-i\phi I_y^{ZQ})$. It makes the x axis of the new frame to coincide
187 with the effective Hamiltonian vector. Note that the Coriolis term in Eq. (15) is zero because U_T is time
188 independent. The effective Hamiltonian can be written as

$$\bar{H}_{eff}^{ZQ} = \omega_{eff}^{ZQ,n} I_x^{eff} \tag{21}$$

$$\omega_{eff}^{ZQ,n} = \sqrt{(\omega_I - \omega_S - n\omega_R)^2 + \frac{1}{4}g_n^2} \tag{22}$$

$$\tan\phi = \frac{\omega_I - \omega_S - n\omega_R}{\frac{1}{2}g_n} \tag{23}$$

189 The initial spin state $\rho^{ZQ}(0) = I_z^{ZQ}$ transforms into $\rho^{eff}(0) = U_T^+ \rho^{ZQ}(0) U_T = \cos\phi\, I_z^{eff} +$
190 $\sin\phi\, I_x^{eff}$ in the effective field frame, and evolves with a frequency $\omega_{eff}^{ZQ,n}$ around the effective field
191 axis I_x^{eff}

$$\rho^{eff}(t) = \cos\phi\left(I_z^{eff}\cos\omega_{eff}^{ZQ,n}t - I_y^{eff}\sin\omega_{eff}^{ZQ,n}t\right) + \sin\phi\, I_x^{eff}$$
$$= \sin\phi\, I_x^{eff} - \cos\phi\sin\omega_{eff}^{ZQ,n}t\, I_y^{eff} + \cos\phi\cos\omega_{eff}^{ZQ,n}t\, I_z^{eff} \tag{24}$$

192 The result is transformed back from the effective field frame into the ZQ subspace as $\rho^{ZQ}(t) =$
193 $U_T \rho^{eff}(t) U_T^+$. This yields

$$
\begin{aligned}
\rho^{ZQ}(t) &= \sin\phi \left(I_x^{ZQ} \cos\phi + I_z^{ZQ} \sin\phi \right) - \cos\phi \sin\omega_{eff}^{ZQ,n} t\, I_y^{ZQ} \\
&\quad + \cos\phi \cos\omega_{eff}^{ZQ,n} t \left(I_z^{ZQ} \cos\phi - I_x^{ZQ} \sin\phi \right) \\
&= \sin\phi \cos\phi \left(1 - \cos\omega_{eff}^{ZQ,n} t \right) I_x^{ZQ} - \cos\phi \sin\omega_{eff}^{ZQ,n} t\, I_y^{ZQ} \\
&\quad + \left(\sin^2\phi + \cos^2\phi \cos\omega_{eff}^{ZQ,n} t \right) I_z^{ZQ}
\end{aligned}
\tag{25}
$$

194 Eq. (25) describes the trajectory of the I_z^{ZQ} operator in the ZQ subspace under the influence of the RF
195 pulses applied in the CP experiment. For evaluation of the magnetization transfer process, only the
196 projection on the I_z^{ZQ} axis is important. We assume that there is no evolution in the DQ subspace, i.e.
197 $\rho^{DQ}(t) = I_z^{DQ}$. The initial I_z operator thus evolves as (recall $I_z = I_z^{ZQ} + I_z^{DQ}$)

$$
\rho^{ZQ}(t) + \rho^{DQ}(t) = \left(\sin^2\phi + \cos^2\phi \cos\omega_{eff}^{ZQ,n} t \right) \frac{1}{2}(I_z - S_z) + \frac{1}{2}(I_z + S_z)
\tag{26}
$$

198 We obtain the CP transfer efficiency in the vicinity of the zero quantum condition (n) by collecting the
199 terms in front of the S_z operator

$$
\begin{aligned}
\epsilon^{ZQ,n} &= \frac{1}{2} \left(1 - \sin^2\phi - \cos^2\phi \cos\omega_{eff}^{ZQ,n} t \right) = \frac{1}{2} \left(\cos^2\phi - \cos^2\phi \cos\omega_{eff}^{ZQ,n} t \right) \\
&= \frac{\cos^2\phi}{2} \left(1 - \cos\omega_{eff}^{ZQ,n} t \right)
\end{aligned}
$$

$$
\epsilon^{ZQ,n} = \frac{1}{2} \frac{\frac{1}{4}g_n^2}{(\omega_I - \omega_S - n\omega_R)^2 + \frac{1}{4}g_n^2} \left[1 - \cos\omega_{eff}^{ZQ,n} t \right]
\tag{27}
$$

200 A similar calculation for the double quantum Hartmann-Hahn condition yields

$$
\epsilon^{DQ,n} = -\frac{1}{2} \frac{\frac{1}{4}g_n^2}{(\omega_I + \omega_S - n\omega_R)^2 + \frac{1}{4}g_n^2} \left[1 - \cos\omega_{eff}^{DQ,n} t \right]
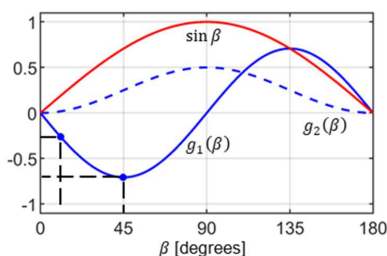\tag{28}
$$

$$
\omega_{eff}^{DQ,n} = \sqrt{(\omega_I + \omega_S - n\omega_R)^2 + \frac{1}{4}g_n^2}
\tag{29}
$$

201 Note the negative sign of the transferred magnetization for the double quantum Hartmann-Hahn
202 transfer. Equations (27) and (28) are identical to the result of an alternative derivation presented by
203 Marica and Snider (Marica and Snider, 2003). The CP MAS matching profile has the form of a Lorentzian
204 function with a width that is dependent on the dipolar coupling b_{IS} and the crystallite orientation
205 (Euler angle β), that are included in the g_n factors. In powders, a quantitative magnetization transfer
206 is not possible as a consequence of the dependence of the size of the effective dipolar coupling on
207 orientation. The magnetization transfer efficiency under MAS is independent of the γ angle. This
208 property is referred to as γ-encoding. The powder average is obtained by evaluation of the integral

$$
\langle \epsilon^{ZQ,n} \rangle_{powder} = \frac{1}{2} \int_0^\pi \epsilon^{ZQ,n} \sin\beta \, d\beta
\tag{30}
$$

MAGNETIC RESONANCE
Open Access
Discussions

209

210

Figure 1. Dipolar coupling scaling factors $g_1(\beta)$ (solid blue line) and $g_2(\beta)$ (dashed blue line) defined in Eqs. (3), (4). The red curve represents the relative probability to find a specific orientation in a powder sample. This weighting factor is employed for the calculation of the transfer efficiencies ϵ in Eq. (30). β angles with β=15° and 45° are used for the visualization of the spin dynamics in the Discussion.

216

2.5. Radiofrequency field inhomogeneity

Radiofrequency fields in MAS probes are realized using solenoid coils. However, a solenoid produces a rather inhomogeneous distribution of magnetic fields across the sample (Tosner et al., 2017). Moreover, as the sample rotates, individual spin packets travel along circles through a spatially inhomogeneous RF field which is determined by the helical geometry of the solenoid coil. This RF inhomogeneity introduces periodic modulations of both the RF amplitude and phase. For the special case of the CP experiment, it was recently shown that these temporal modulations have a negligible effect (Aebischer et al., 2021) and will be ignored in the present treatment. In addition, the distribution of the RF fields depends on the frequency (Engelke, 2002), and can be influenced by different balancing of the RF circuitry on different channels (Paulson et al., 2004). For simplicity, we assume the RF field distributions to be equal for the I and S spins and disregard the radial dependency. The effect of RF field inhomogeneity on the CP experiment was previously studied by Paulson et al. (Paulson et al., 2004), and Gupta et al. (Gupta et al., 2015). An example of the distribution of the RF field along the coil axis, denoted $\xi(z)$, is shown in Figure 2. As noted by Gupta et al., the profile deviates from a Gaussian function and is well described by a power law dependence. In our study, we use the B_1 profile calculated according to Engelke (Engelke, 2002).

The distribution of RF field amplitudes enters the formulas of the CP experiment using the substitution

$$\omega_I \xrightarrow{\text{replace}} \xi(z)\omega_I^{NOM}$$
$$\omega_S \xrightarrow{\text{replace}} \xi(z)\omega_S^{NOM} \tag{31}$$

where ω_I^{NOM}, ω_S^{NOM} refer to the nominal RF amplitudes realized in the center of the coil ($z = 0$ where $\xi(0) = 1$). The overall experimental efficiency corresponds to the integral over the sample volume weighted by the detection sensitivity of the coil. According to the reciprocity theorem (Hoult, 2000),

237   the sensitivity is proportional to the RF field. We assume that the sample extends over a length l, and
238   is placed symmetrically within the solenoid coil.

$$\langle \epsilon^{ZQ,n} \rangle_{powder}^{rf-inh} = \frac{1}{w} \int_{-l/2}^{+l/2} \langle \epsilon^{ZQ,n} \rangle_{powder} \, \xi(z) dz \qquad (32)$$

239   The normalization factor w is given as

$$w = \int_{-l/2}^{+l/2} \xi(z) dz \qquad (33)$$

240   It is not possible to match the Hartmann-Hahn conditions for the whole sample volume. Assuming that
241   the zero-quantum condition is fulfilled for the nominal rf amplitudes, i.e., $\omega_I^{NOM} - \omega_S^{NOM} = n\omega_R$, we
242   get

243    $\qquad \omega_I - \omega_S - n\omega_R = \xi(z)\big(\omega_I^{NOM} - \omega_S^{NOM}\big) - n\omega_R = \xi(z)n\omega_R - n\omega_R = n\omega_R(\xi(z) - 1)$

244   and

$$\bar{H}^{ZQ} = n\omega_R[\xi(z) - 1]I_z^{ZQ} + \frac{1}{2}g_n I_x^{ZQ} \qquad (34)$$

245   Eq. (34) shows that in the case of an inhomogeneous RF field, the prevailing component along the I_z^{ZQ}
246   operator in the effective Hamiltonian $\bar{H}^{ZQ}$ is proportional to the MAS frequency ω_R, multiplied by the
247   order of the recoupling condition n. The effect of RF amplitude mismatch on spin dynamics is more
248   pronounced for small dipolar couplings, b_{IS}, which is reflected in the width of the CP MAS matching
249   profiles derived above. Thus, we could analytically derive a dependence of the performance of the CP
250   experiment on the MAS frequency.
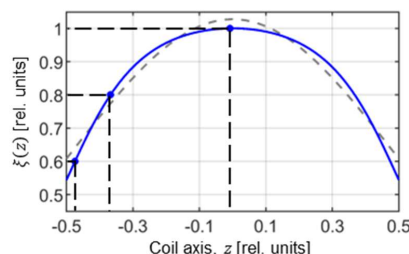
251

252   **Figure 2**: RF field inhomogeneity profile along the axis of a solenoid coil. The profile is calculated
253   according to Engelke (Engelke, 2002) assuming a coil length of 7.9 mm, a diameter of 3.95 mm, and
254   assuming 7 turns (blue line). The grey dashed line represents a fit of the RF profile assuming a Gaussian
255   function suggested by Paulson et al. (Paulson et al., 2004). The power law relation introduced by Gupta
256   et al. (Gupta et al., 2015) yields a perfect fit of the theoretical behavior and exactly matches the blue
257   curve. Values ξ=0.6, 0.8, and 1.0 are used in the Discussion session to visualize spin dynamics.

258

259   ### 2.6. Linear ramp and adiabatic sweep

260   The most popular way to overcome the limitations of the constant amplitude CP and the RF mismatch

261   at different positions of the sample is the use of a linear ramp or an adiabatic tangential sweep on one

262   of the RF channels. We can define

$$\omega_I^{NOM} = \omega_I^0 + f(t) \tag{35}$$

263   where the function $f(t)$ describes the sweep from $-\Delta/2$ to $+\Delta/2$ over time $t \in \langle 0, T \rangle$. The function

264     $f(t)$ can be defined for the linear ramp as

$$f(t) = \Delta \left(\frac{t}{T} - \frac{1}{2} \right) \tag{36}$$

265   and for tangential sweep as

$$f(t) = b \tan \left[\left(\frac{2t}{T} - 1 \right) \arctan \frac{\Delta}{2b} \right] \tag{37}$$

266   where b parametrizes the curvature of the sweep. Values for b are typically in the range of $\frac{\Delta}{1000} < b <$

267   Δ. For $b = \frac{\Delta}{1000}$, $f(t)$ is almost constant except for the end points where the function rapidly changes

268   from/to $\mp\Delta/2$. For $b = \Delta$, $f(t)$ approaches the linear ramp. The influence of b on the shape is

269   illustrated in Figure 3. During a truly adiabatic transfer, the effective field is aligned with the initial

270   magnetization along the $+I_z^{ZQ}$ axis, and changes its orientation slowly towards $-I_z^{ZQ}$. The spin state is

271   locked along the effective field and is inverted as well (Hediger et al., 1995). The adiabaticity condition

272   is given as

$$\frac{d}{dt} \phi(t) \ll \omega_{eff} \tag{38}$$

273   where ω_{eff} is defined in Eq. (22), and the angle ϕ is given in Eq. (23). Adiabatic inversion pulses have

274   been an integral part of the NMR toolbox for a long time (Baum et al., 1985). There is, however, a

275   substantial difference between broadband inversion pulses and cross-polarization. Inversion pulses

276   allow to manipulate the effective field along both z and x directions, corresponding to offset and RF

277   amplitude, respectively. In the CP experiment, the x axis component of the effective Hamiltonian is

278   fixed and is determined by the dipolar coupling, see Eq. (19) and Eq. (20). In addition, perfect alignment

279   of the effective field with the initial state is difficult to achieve as the RF amplitudes are restricted to

280   the vicinity of the Hartmann-Hahn condition.

281

MAGNETIC RESONANCE
Open Access Discussions

282
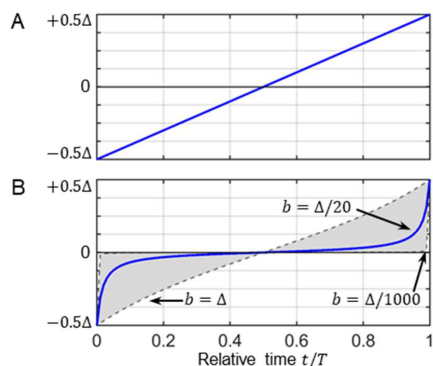
Figure 3: RF amplitude sweeps employed in cross-polarization experiments for (A) a linear ramp and
(B) an adiabatic tangential sweep. Eq. (36) and (37) mathematically describe the time dependent RF
amplitude. The parameter b determines the curvature of the adiabatic tangential shape.

286

2.7. RF amplitude sweeps and RF field inhomogeneity

In the following, we aim to include RF field inhomogeneity in the description of the RF amplitude sweep
of Eq. (35). We assume that the zero quantum Hartmann-Hahn matching conditions are fulfilled in the
middle of the sweep and in the center of the coil for the nominal RF field amplitudes, i.e. for $\omega_I^0 - \omega_S^{NOM} = n\omega_R$. The I_z^{ZQ} component of the Hamiltonian $\bar{H}^{ZQ}$ then becomes

$$
\begin{aligned}
\omega_I - \omega_S - n\omega_R &= \xi(z)[\omega_I^{NOM} - \omega_S^{NOM}] - n\omega_R \\
&= \xi(z)[\omega_I^0 + f(t) - \omega_S^{NOM}] - n\omega_R = \xi(z)[f(t) + n\omega_R] - n\omega_R \quad (39) \\
&= \xi(z)f(t) + n\omega_R[\xi(z) - 1]
\end{aligned}
$$

and

$$
\bar{H}^{ZQ} = \{\xi(z)f(t) + n\omega_R[\xi(z) - 1]\}I_z^{ZQ} + \frac{1}{2}g_n I_x^{ZQ} \quad (40)
$$

Now, the sweep function $f(t)$ is scaled by the RF field inhomogeneity factor $\xi(z)$. At the same time,
the center of the sweep is shifted by an amount proportional to the MAS frequency ω_R. In Figure 4,
the sweep range is depicted in green as a function of position along the coil axis. Spins located in
volume elements towards the ends of the coil where the RF field is smaller experience RF amplitude
sweeps that do not cover the recoupling condition at all (e.g. for ξ=0.8 in Figure 4A). This is another
example of how increased MAS frequencies impact the cross-polarization experiment and cause a
decrease in performance.

When setting the numerical values of RF amplitudes ω_I^0, ω_S^{NOM}, and the sweep range Δ, it can happen
that double-quantum conditions are fulfilled in some places within the sample when the values are
scaled by the RF field inhomogeneity. The double quantum conditions are governed by the formula

$$\begin{aligned}
\omega_I + \omega_S - n\omega_R &= \xi(z)\left[\omega_I^{NOM} + \omega_S^{NOM}\right] - n\omega_R \\
&= \xi(z)\left[\omega_I^0 + f(t) + \omega_S^{NOM}\right] - n\omega_R \\
&= \xi(z)f(t) + \xi(z)\left(\omega_I^0 + \omega_S^{NOM}\right) - n\omega_R
\end{aligned} \tag{41}$$

303 which is represented in red in Figure 4C. While the values ω_I^0, ω_S^{NOM} are satisfying the zero quantum
304 $n = +1$ condition around the center of the coil, at the same time, they satisfy the double quantum
305 $n = +2$ condition towards the ends of the coil (places where the red area crosses zero value). As a
306 result, there are parts of the sample that produce positive magnetization transfer and parts that
307 experience negative transfer. Thus, the overall efficiency of the experiment is decreased.

308
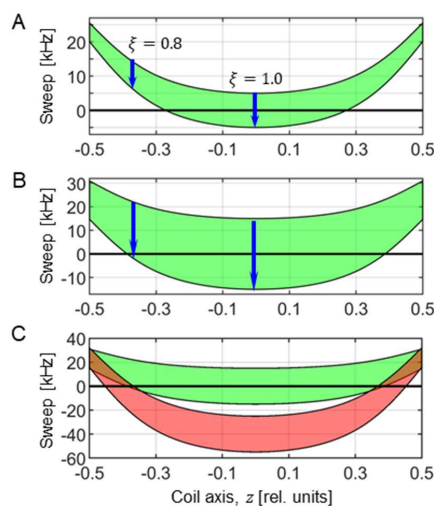
309

310 **Figure 4**: Visualization of the RF sweep ranges as a function of the position of a particular spin packet
311 along the coil axis. The Hartmann-Hahn resonance condition is artificially defined for a sweep
312 frequency 0 kHz. (A) The sweep range (green area) is evaluated according to Eq. (39) for $n = +1$ and
313 assuming an MAS frequency of 50 kHz. The blue arrows indicate the direction of the sweep for an RF
314 inhomogeneity factor of ξ=0.8 and 1.0. The sweep amplitude Δ corresponds to 10 kHz and 30 kHz in
315 (A) and (B), respectively. (C) Overlay of the RF amplitude sweeps evaluated for the ZQ ($n = +1$)
316 matching condition (Eq. (39), green) and DQ ($n = +2$) matching condition (Eq. (41), red) with nominal
317 RF amplitudes $\omega_I^{NOM}/2\pi$=95 kHz and $\omega_S^{NOM}/2\pi$=45 kHz. These values were selected to demonstrate
318 that the ZQ matching condition is satisfied in the center of the coil, and simultaneously a DQ is
319 encountered for spin packets in regions of the sample where the RF amplitudes are scaled down by
320 the RF field inhomogeneity.

321

MAGNETIC
RESONANCE
Discussions

3. Results and Discussion

3.1. CP matching profile

Experimentally, optimal cross polarization conditions are found in experiments in which the RF amplitude on one of the RF channels is systematically varied to yield the highest sensitivity. In case the Hartmann-Hahn recoupling condition is very narrow, this can be difficult as many repetitions with a small increment of the RF amplitude are required. In the Theory section, we derived analytical formulas for the CP matching profiles for constant RF amplitudes. We have found that for a homogeneous RF field distribution, the width at half height of the recoupling condition is governed by the size of the dipolar coupling and can be estimated as $0.468 b_{IS}$ after powder averaging. Both the width and the maximal transfer efficiency are independent of the MAS frequency. Maximum transfer of 73% is achieved for mixing times satisfying the condition $t b_{IS} = 1.7$ for the $n = \pm 1$ recoupling conditions. The same efficiency is obtained for the $n = \pm 2$ conditions. However, due to the different spatial dependence and scaling factors in g_1 and g_2 terms (Eqs. (3) and (4)) the maximum is achieved there for mixing times $t b_{IS} = 2.4$. These facts are well known and are presented graphically in Figure 5. Figure 5A shows the CP matching profile calculated using Eq. (27) and (30) for $n = +1$ and assuming a dipolar coupling constant b_{IS} of 1, 10, and 20 kHz, which are the characteristic values for ^{13}C-^{15}N, ^{1}H-^{15}N, and ^{1}H-^{13}C spin pairs, respectively. $\langle \epsilon^{ZQ,+1} \rangle_{powder}$ is represented as a function of the RF amplitude mismatch $\delta_M / 2\pi = \omega_I - \omega_S - \omega_R$ with respect to the exact Hartmann-Hahn.
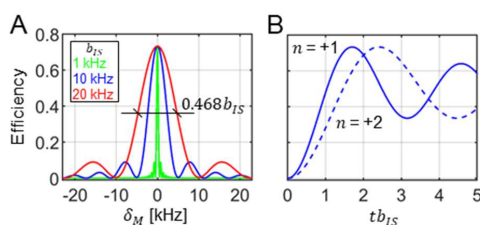
Figure 5: Properties of the constant amplitude CP experiment assuming homogeneous RF fields. (A) The width of the CP matching profile around the zero-quantum (n=+1) Hartmann-Hahn matching condition depends on the dipolar coupling strength b_{IS}. (B) Magnetization buildup of the transferred magnetization for the n=+1 and n=+2 matching condition. Independently of the MAS frequency and b_{IS}, the n=+2 condition reaches the same maximum, however, at longer mixing times. The curves were calculated using Eqs. (27) and (30).

For inhomogeneous RF fields, the CP matching profile can be quantitatively described by inserting Eq. (31) into Eq. (27) and taking the average in Eq. (32). Figure 6A shows the influence of inhomogeneous RF fields and the induced asymmetric broadening of the matching profile $\langle \epsilon^{ZQ,+1} \rangle_{powder}^{rf-inh}$. Clearly, the maximal transfer efficiency substantially decreases with increasing MAS frequency.

353 A closer inspection of the CP matching profiles in Figure 6A reveals that the maximum overall transfer
354 efficiency is not reached for the exact ZQ ($n = +1$) condition with $\omega_I^{NOM} - \omega_S^{NOM} = \omega_R$,
355 corresponding to $\delta_M= 0$. In practice, it is advantageous to set ω_I^{NOM} little higher and thus shift the
356 volume element where the Hartmann-Hahn condition is matched away from the center of the coil.
357 This allows to partially compensate for the destructive effect of the RF field inhomogeneity. This
358 mismatch δ_M of the Hartmann-Hahn matching condition is naturally found during the experimental
359 setup when the RF fields are optimized to experimentally yield the best efficiency. However, the
360 mismatch is small (a few kHz at most) and generally decreases with decreasing MAS frequency (see
361 the dashed line in Figure 6A). Similarly, the RF field inhomogeneity has a subtle effect on the buildup
362 of the transferred magnetization. Figure 6B shows that maximum transfer occurs at shorter mixing
363 times for increased MAS frequencies.

364 Figure 6C shows how decreasing dipolar couplings result in a diminished Hartmann-Hahn transfer
365 efficiency. The calculations are carried out for three typical dipolar coupling values, and for MAS
366 frequencies in the range of 20 kHz to 200 kHz. Strikingly, for $\omega_R/2\pi$=200 kHz and b_{IS}=1 kHz, the
367 maximum transfer is only about 7%.

368 We used numerical simulations in SIMPSON (Bak et al., 2000; Tosner et al., 2014) to verify the
369 predictions of the analytical model. To implement an experiment, specific values of ω_I and ω_S need to
370 be selected. Consideration of RF field inhomogeneity increases the complexity of this selection process,
371 since certain values of ω_I, ω_S can lead to a situation in which ZQ and DQ recoupling conditions are
372 fulfilled simultaneously in different parts of the sample (Figure 4C). This phenomenon was explored
373 experimentally by Gupta et al. (Gupta et al., 2015). In case this situation is avoided, we find perfect
374 agreement between the analytical model and the numerical simulations (data not shown).

375

376
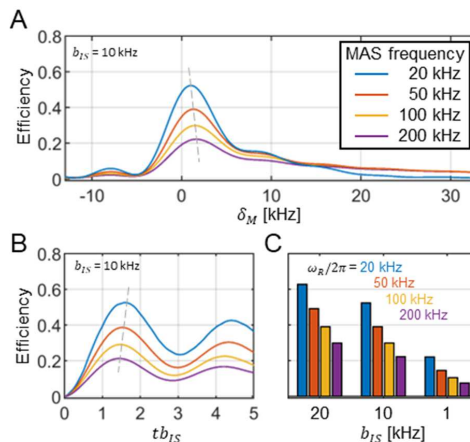
Figure 6: Transfer efficiency of the constant amplitude CP experiment in the presence of RF field
inhomogeneity and assuming a dipolar coupling strength b_{IS} = 10 kHz. For the calculation, a rotor fully
packed with material is assumed. (A) The maximum of the CP matching profile decreases with
increasing MAS frequency for the zero-quantum (n=+1) condition. At the same time, the width

381 increases. A grey dashed line is used to indicate the position of the maximum. The maximum of the CP
382 matching profile shifts to higher mismatch values δ_M for increased MAS frequencies. (B) Magnetization
383 buildup curves for different MAS frequencies. The legend is indicated in panel (A). With increasing MAS
384 frequencies, magnetization reaches the maximum transfer at shorter mixing times. (C) Maximum
385 transfer efficiencies for the characteristic dipolar coupling values b_{IS} of 1, 10 and 20 kHz for different
386 MAS frequencies. Data were generated using Eqs. (27), (31) and (32).

387

388 ### 3.2. Visualization of the magnetization transfer trajectories

389 In the following, we aim to visualize the spin trajectory during the CP experiment in its basic form with
390 constant RF and with RF amplitude sweeps. We focus on the vicinity of the ZQ ($n = +1$) Hartmann-
391 Hahn condition and use the effective Hamiltonian $\bar{H}^{ZQ}$ given in Eq. (34) for the analysis. We consider
392 RF field inhomogeneity and assume nominal RF amplitudes that match the recoupling condition in the
393 center of the coil, $\omega_I^{NOM} - \omega_S^{NOM} = \omega_R$. Figure 7 shows the spin dynamics for two crystallite
394 orientations (β=15° and 45°), and three positions within the coil (ξ=0.6, 0.8, and 1.0). These conditions
395 are highlighted in Figure 1 and Figure 2. In the center of the coil where ξ=1.0, the Hamiltonian $\bar{H}^{ZQ}$
396 (blue vector) is aligned with the I_x^{ZQ} axis. The spin state vector $\rho^{ZQ}(t)$ (red vector) rotates in circles
397 within the yz plane with an angular velocity that depends on the crystallite orientation (Figure 7C,F).
398 This situation corresponds to the case without RF field inhomogeneity.

399 Depending on the position within the coil, a mismatch contribution in the effective Hamiltonian $\bar{H}^{ZQ}$
400 along the I_z^{ZQ} axis is obtained, which is according to Eq. (34) proportional to the MAS frequency. The
401 effective rotation axis is tilted away from the I_x^{ZQ} direction by an angle ϕ, Eq. (23). The effective
402 rotation frequency $\omega_{eff}^{ZQ,+1}$, Eq. (22), increases with increasing mismatch. Likewise, the I_x^{ZQ} component
403 of $\bar{H}^{ZQ}$ decreases with the decreasing effective dipolar coupling. This amplifies the effect of the RF
404 field inhomogeneity on the orientation of the effective Hamiltonian axis. The state vector rotates on
405 the surface of a cone (Figure 7AB,DE). As a consequence, the inversion becomes inefficient. Only the
406 central part of the sample yields a high transfer efficiency.
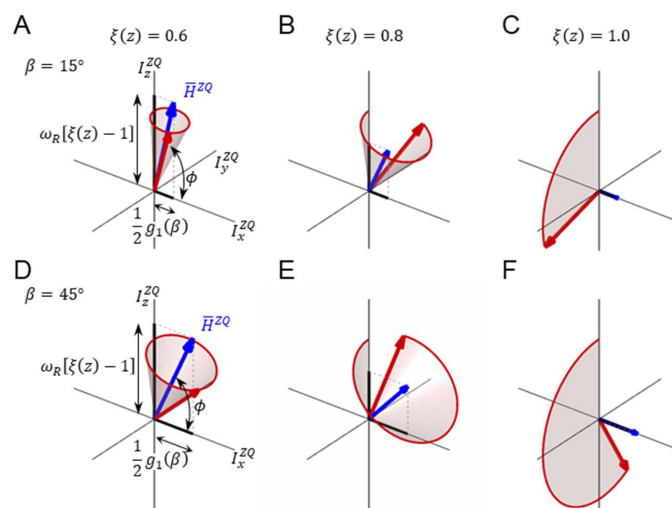
Figure 7. Visualization of the spin state trajectories for the constant amplitude cross-polarization experiment evaluated for two crystal orientations. (A-C) crystallite orientation β=15°, (D-F) β=45°. The calculations were carried out for 3 positions along the coil axis that correspond to RF field scaling values of $\xi(z)$=0.6 (panels A/D), 0.8 (panels B/E), and 1.0 (panels C/F). The state vector, ρ^{ZQ}, is represented by a red vector. The effective Hamiltonians are represented by blue vectors. ρ^{ZQ} rotates around $\bar{H}^{ZQ}$ on the surface of a cone (shaded area). In the simulation, an MAS frequency of 50 kHz and b_{IS}=10 kHz was assumed.

3.3. RF amplitude sweeps in the absence of RF field inhomogeneity

Continuous RF amplitude sweeps are used to improve the cross polarization efficiency. In this case, the effective Hamiltonian changes its orientation in the course of the pulse sequence. An adiabatic inversion is achieved if two conditions are fulfilled: (i) the initial state vector is aligned with the initial effective field vector and (ii) the effective field changes its orientation slowly. We focus on the zero quantum ($n = +1$) condition assuming a dipolar coupling constant b_{IS}= 10 kHz. In the following, spin state trajectories are calculated for two sweep amplitudes, Δ = 10 kHz and 30 kHz.

The spin state trajectories for the linear ramp are represented in Figure 8. The I_x^{ZQ} component of the effective Hamiltonian is fixed in time, and is given by the effective dipolar coupling at a given orientation (Eq. (40), assuming ξ=1.0). The maximal value of $\frac{1}{2}g_1(\beta)$ is reached for β=45° which together with the sweep amplitude of Δ=10 kHz and according to Eq. (23) results in a tilt angle of the effective field $\phi(t = 0, \beta = 45°)$=54.7° at the beginning of the pulse sequence (Figure 8B). Clearly, the initial state vector $\rho^{ZQ}(0) = I_z^{ZQ}$ is not aligned with the effective field of $\bar{H}^{ZQ}(t = 0)$. However, the inversion efficiency is high due to the slow change of the orientation of the effective field, $d\phi/dt$, such that the state vector can follow the effective field while it is rotating around it in rather large circles (see evaluation of the adiabaticity condition in Figure 8F). For a smaller effective dipolar coupling (for example, β=15° in Figure 8A), the angle ϕ is larger, close to 90°. During the linear ramp, the effective

17

433 Hamiltonian amplitude $\omega_{eff}^{ZQ}(t)$ goes through a minimum in the middle of the sweep at $t = T/2$, where

434 its value is solely determined by the effective dipolar coupling, see Eq. (22). At the same time, $d\phi/dt$

435 reaches its maximum (Figure 8E). Under these conditions, the state vector keeps track with the

436 effective field (Figure 8A). When a larger sweep amplitude is employed, e.g. Δ=30 kHz, the orientation

437 of the initial effective field is closer to the I_z^{ZQ} axis, $\phi(t = 0, \beta = 45°)$=76.7° (Figure 8D). At the same

438 time, the amplitude of the effective Hamiltonian $\omega_{eff}^{ZQ}(t = 0)$ is increased as well. For the crystallite

439 orientation β=15° (Figure 8C), however, we find that the adiabaticity condition is violated in the middle

440 of the pulse sequence (Figure 8G). The state vector is not able to follow the effective field as $d\phi/dt$

441 becomes too high. As a consequence, the state vector keeps rotating near the equator (Figure 8C) and

442 thus contributes little to the total transfer efficiency.
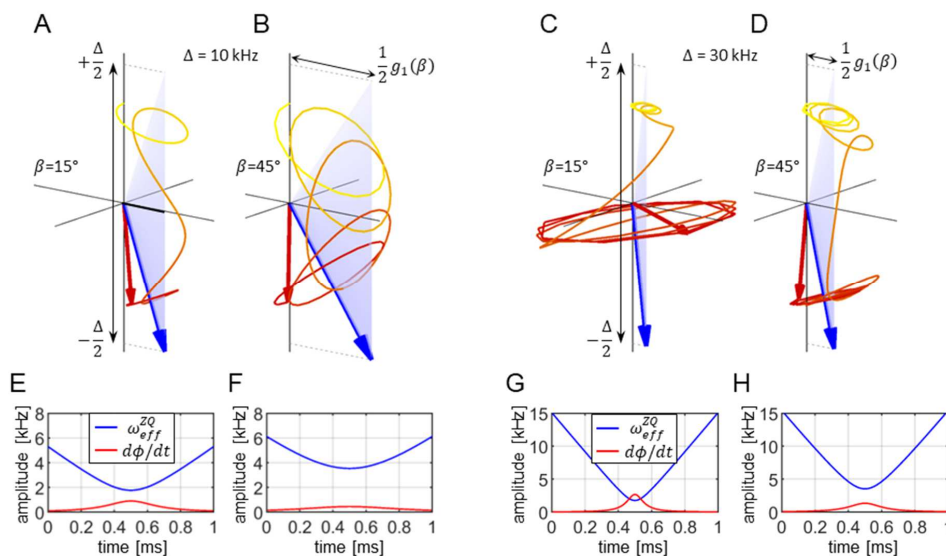
443

444 **Figure 8**. Visualization of the spin state trajectories for the linear ramp cross-polarization experiment

445 assuming a homogeneous RF field distribution. For the simulation, a dipolar coupling b_{IS}=10 kHz was

446 assumed. The CP contact time was set to T=1 ms. The calculation was carried out for two crystallite

447 orientations (β=15° and 45°, panels A,C and B,D, respectively), and two sweep amplitudes (Δ=10 kHz

448 and Δ=30 kHz, panels A,B and C,D, respectively). The blue-shaded areas represent the changing

449 effective Hamiltonian. The blue arrow indicates the effective Hamiltonian at the end of the pulse

450 sequence at $t = T$. The component along the I_z^{ZQ}-axis is time dependent, while the I_x^{ZQ}-axis

451 component is fixed (see Eq. (40)). The beginning of the trajectory is depicted as a yellow line which

452 gradually turns into red as the trajectory progresses. The final state of the spin state vector (initially

453 oriented along I_z^{ZQ}) is drawn as a red arrow. Panels E-H display $d\phi(t)/dt$ and $\omega_{eff}^{ZQ}(t)$. In C/G, the

454 adiabaticity condition $d\phi/dt<\omega_{eff}$ is violated during the sweep.

455

456 Spin state trajectories for the adiabatic variant of the CP experiment are shown in Figure 9. The

457 tangential sweep has been suggested to keep the rate of change $d\phi(t)/dt$ small compared to the

458   effective field amplitude at all times (Hediger et al., 1995). Initially, $\omega_{eff}(t)$ is large implicating that
459    $d\phi(t)/dt$ can be large. However, for small sweep amplitudes such as Δ=10 kHz the effective field
460   changes too rapidly for a portion of crystallites at the beginning and at the end of the sweep so that
461   the adiabaticity condition is violated (Figure 9E). Most of the dynamics takes place when the tangential
462   function goes through the central plateau, where the RF amplitudes do not change significantly over
463   an extended period of time. The state vector rotates in large circles around the effective Hamiltonian
464   that is oriented predominantly along the I_x^{ZQ} axis. When a larger sweep amplitude $\Delta = 30$ kHz is used,
465   the adiabatic regime is restored for most crystallite orientations and an improved transfer efficiency is
466   obtained.

467   Figure 10 compares the magnetization transfer during the RF sweep for the examples discussed above.
468   The transfer process is fast when the change of the effective field orientation is fast: in the middle of
469   the linear ramp, and at the beginning and at the end of the tangential sweep, provided the adiabaticity
470   condition is maintained (Figure 10AB). Figure 10CD shows the transfer efficiency as a function of
471   crystallite orientation. Note that the spin state inversion cannot be achieved for crystallite orientations
472   with an effective dipolar coupling that is vanishing, i.e., for β=0° and 90°. The portion of crystallites
473   yielding low transfer depends on the ratio of the sweep amplitude Δ and the dipolar coupling b_{IS}. For
474   the linear ramp Δ=10 kHz is preferable, while the tangential sweep using an amplitude Δ = 30 kHz yields
475   high efficiency for most of the crystallites under the conditions investigated here. After powder
476   averaging, the magnetization transfer efficiency is on the order of 90% for the tangential sweep. We
477   would like to note that all predictions based on the ZQ average Hamiltonian agree well with exact
478   simulations using SIMPSON (data not shown).

479
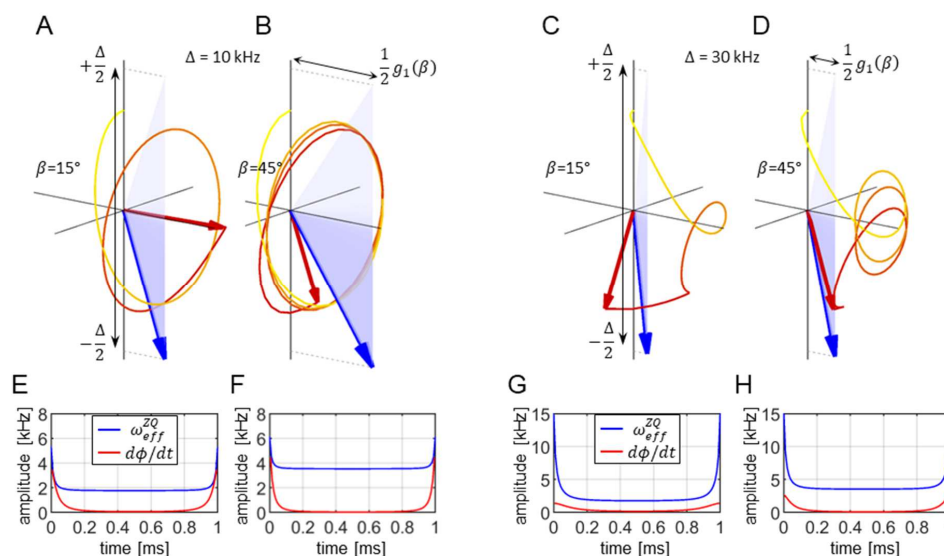
481   **Figure 9:** Visualization of the spin state trajectories for the adiabatic tangential sweep cross-
482   polarization experiment assuming a homogeneous RF field distribution. For the simulation, a dipolar

483 coupling b_{IS}=10 kHz was assumed. The CP contact time was set to T=1 ms. The calculation was carried

484 out for two crystallite orientations (β=15° and 45°, panels A,C and B,D, respectively) and two sweep

485 amplitudes (Δ=10 kHz and Δ=30 kHz, panels A,B and C,D, respectively, $b = \Delta/50$). The blue-shaded

486 areas represent the changing effective Hamiltonian. The blue arrow indicates the effective Hamiltonian

487 at the end of the pulse sequence at $t = T$. The component along the I_z^{ZQ}-axis is time dependent, while

488 the I_x^{ZQ}-axis component is fixed (see Eq. (40)). The beginning of the trajectory is depicted as a yellow

489 line which gradually turns into red as the trajectory progresses. The final state of the spin state vector

490 (initially oriented along I_z^{ZQ}) is drawn as a red arrow. Panels E-H display $d\phi(t)/dt$ and $\omega_{eff}^{ZQ}(t)$. In A/E

491 and B/F, the adiabaticity condition $d\phi/dt < \omega_{eff}$ is violated during the sweep.

492
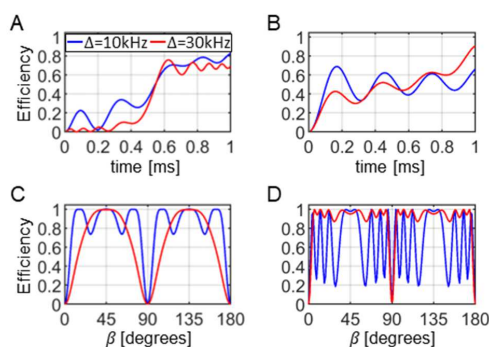
Figure 10: Powder averaged buildup of the transferred magnetization during the mixing time of the CP experiment (A, B) and the final transfer efficiency as a function of crystallite orientation (C, D) for an RF amplitude sweep using a linear ramp (A,C) and a tangential shape (B, D). The blue and red curves correspond to sweep amplitudes of 10 and 30 kHz, respectively. In all simulations, a homogeneous RF field distribution is assumed.

499

### 3.4. RF amplitude sweeps in the presence of an inhomogeneous RF field

501 In the following paragraph, RF field inhomogeneities are included in the analysis. For simplicity, we

502 assume that the RF field varies along the solenoid coil axis as described in Figure 2 and is the same for

503 both RF channels. We disregard time modulations induced by sample rotation in a spatially

504 inhomogeneous RF field. We assume that the Hartmann-Hahn condition is fulfilled for the nominal RF

505 amplitudes in the middle of the coil. The RF amplitude sweep is applied to the I channel. We again

506 examine the zero-quantum ($n = +1$) recoupling condition. The drive Hamiltonian $\overline{H}^{ZQ}$ is given by Eq.

507 (40). Sweeping the RF amplitude makes the I_z^{ZQ}-component of the effective Hamiltonian time

508 dependent. The range over which it varies depends on the position along the coil axis, and it is

509 visualized in Figure 4. The center of the sweep is shifted away from the exact matching condition

510 towards the ends of the coil by an amount that depends on the MAS frequency. As discussed above,

511 the evolution in the double-quantum subspace can be neglected, since $\overline{H}^{DQ}$ has a dominant

512 component along I_z^{DQ} axis which is much larger than the effective dipolar coupling. This can be

513 achieved by choosing a proper value for ω_S^{NOM}. At the same time, we have chosen conditions that

514 avoid simultaneous matching of different Hartmann-Hahn conditions within the sample volume.

515 The previous description of the RF amplitude modulated CP is valid in the center of the coil where

516 ξ=1.0. The situation is quite different in volume elements towards the ends of the coil. Figure 11

517 illustrates the spin state trajectories for the linear ramp CP experiment, assuming a crystallite angle

518 β=45°, a MAS frequency of $\omega_R/2\pi$=50 kHz, and a dipolar coupling constant of b_{IS}= 10 kHz. The scaling

519 factor ξ=0.8 is realized for $z = \pm 0.36l$ (where l is the coil length) around the center of the coil. When

520 the sweep amplitude is Δ=10 kHz, the effective field does not get inverted during the sweep (Figure 4A

521 and Figure 11A) and therefore cannot invert the spin state, regardless of its adiabaticity (Figure 11E).

522 Increasing the sweep amplitude to Δ=30 kHz yields better results as the effective field approaches the

523 Hartmann-Hahn recoupling condition towards the end of the sweep period (Figure 4B and Figure 11C).
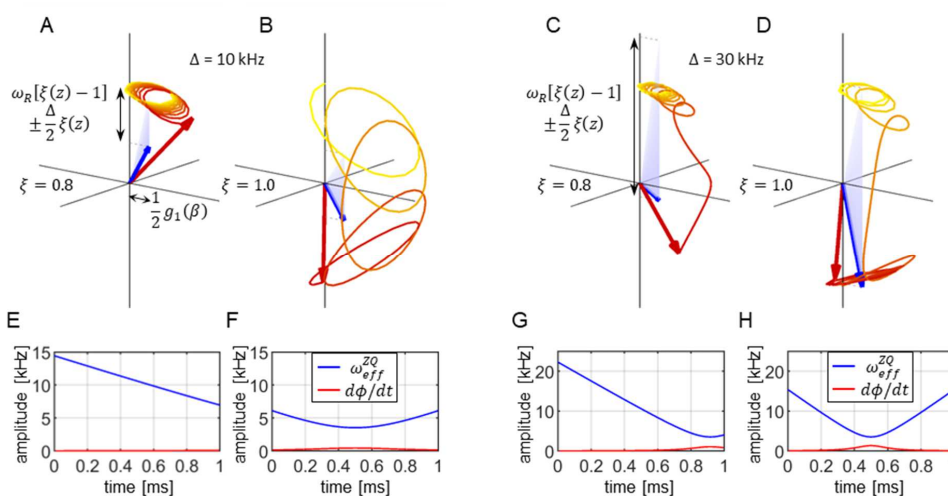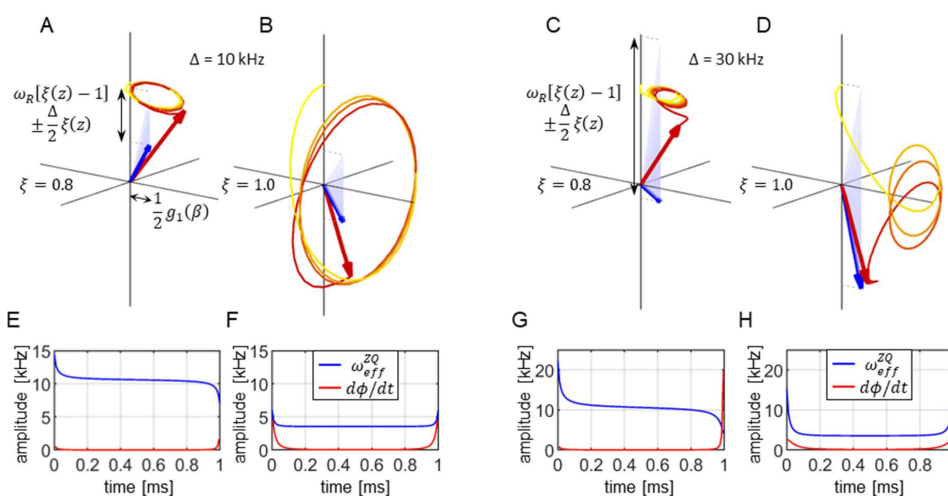

524

525 **Figure 11:** Visualization of the spin state trajectory for a linear ramp cross-polarization experiment

526 assuming an inhomogeneous RF field distribution. For the simulation, a dipolar coupling b_{IS}=10 kHz

527 was assumed. The CP contact time was set to T=1 ms. The calculation was carried out for one crystallite

528 orientation (β= 45°) and two positions along the coil axis with RF field scaling factors ξ=0.8 and 1.0

529 (panels A,C and B,D) and two sweep amplitudes Δ=10 kHz and Δ=30 kHz (panels A,B and C,D). The blue-

530 shaded areas represent the changing effective Hamiltonian. The blue arrow indicates the effective

531 Hamiltonian at the end of the pulse sequence at $t = T$. The component along the I_z^{ZQ}-axis is time

532 dependent, while the I_x^{ZQ}-axis component is fixed (see Eq. (40)). The beginning of the trajectory is

533 depicted as a yellow line which gradually turns into red as the trajectory progresses. The final state of

534 the spin state vector (initially oriented along I_z^{ZQ}) is drawn as a red arrow. Panels E-H display $d\phi(t)/dt$

535 and $\omega_{eff}^{ZQ}(t)$ to appreciate whether the adiabaticity condition $d\phi/dt < \omega_{eff}$ is violated during the

536 sweep.

537

538   For a tangential sweep, the spin state trajectories are depicted in Figure 12. Initially, and towards the
539   end of the sweeping period, the RF amplitude changes rapidly and so does the effective field
540   orientation. This can lead to a violation of the adiabaticity condition, as encountered for the calculation
541   with a sweep amplitude of Δ=30 kHz (Figure 12C,G). Despite the fact that the Hartmann-Hahn matching
542   condition is included within the sweep range, the state vector does not follow the effective field. These
543   parts of the sample yield a low transfer efficiency.

544

545

Figure 12: Visualization of the spin state trajectory for an adiabatic tangential sweep cross-polarization
experiment assuming an inhomogeneous RF field. For the simulation, a dipolar coupling b_{IS}=10 kHz
was assumed. The CP contact time was set to T=1 ms. The calculation was carried out for one crystallite
orientation (β= 45°) and two positions along the coil axis with RF field scaling factors ξ=0.8 and 1.0
(panels A,C and B,D) and two sweep amplitudes Δ=10 kHz and Δ=30 kHz, assuming $b = \Delta/50$ (panels
A,B and C,D). The blue-shaded areas represent the changing effective Hamiltonian. The blue arrow
indicates the effective Hamiltonian at the end of the pulse sequence at $t = T$. The component along
the I_z^{ZQ}-axis is time dependent, while the I_x^{ZQ}-axis component is fixed (see Eq. (40)). The beginning of
the trajectory is depicted as a yellow line which gradually turns into red as the trajectory progresses.
The final state of the spin state vector (initially oriented along I_z^{ZQ}) is drawn as a red arrow. Panels E-
H display $d\phi(t)/dt$ and $\omega_{eff}^{ZQ}(t)$ to appreciate whether the adiabaticity condition $d\phi/dt<\omega_{eff}$ is
violated during the sweep.

558

559   The buildup of the transferred magnetization integrated over the sample volume and detected by the
560   NMR coil for both the linear ramp and the tangential sweep is presented in Figure 13A,B. It is not
561   obvious which sweeping method will yield a higher total transfer efficiency. Of the four setups
562   discussed so far, the linear ramp with Δ=30 kHz yields the best result. When comparing efficiency
563   profiles along the coil axis (Figure 13C,D) we observe that tangential sweep is more efficient near the

564 center of the coil but quickly loses efficiency when going towards the ends. However, linear ramp yields
565 equal transfer over a larger sample volume.

566
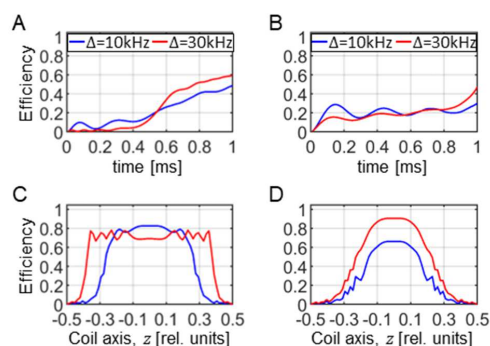
567

568 **Figure 13**: Powder averaged buildup of transferred magnetization during the mixing time of the CP
569 experiment (A, B), and the final powder averaged transfer efficiency as a function of the position along
570 the coil axis (C, D) for a linear ramp (A,C) and a tangential shape (B, D). The blue and red curves
571 correspond to sweep amplitudes of Δ=10 kHz and Δ=30 kHz, respectively. In the calculation, an
572 inhomogeneous RF field is assumed.

573

574 ### 3.5. Numerical optimizations of linear and tangential sweeps

575 In this section, we discuss which parameters of a linear ramp and a tangential sweep yield the best
576 transfer efficiency. We address this problem by a numerical optimization. The calculations are
577 repeated for a range of dipolar couplings and MAS frequencies. In the case of the linear ramp, the
578 sweep amplitude Δ and the offset δ_M from the exact Hartmann-Hahn condition are optimized. In case
579 of the tangential sweep, the curvature parameter b is considered in addition (Figure 3). The offset
580 parameter δ_M corresponds to the mismatch of the recoupling condition in the middle of the coil due
581 to RF inhomogeneity and reflects the experimental optimization procedure where the amplitude
582 ω_S^{NOM} is kept constant and the amplitude ω_I^0 is optimized around the expected recoupling condition.
583 To ensure that not more than one matching condition is encountered during the sweep, the amplitude
584 Δ was restricted to values within $\pm \omega_R/2$ (Hediger et al., 1995). The dynamics was evaluated using the
585 effective Hamiltonian $\bar{H}^{ZQ}$ given in Eq. (40). The optimized parameters correspond to the best transfer
586 efficiency obtained from 100 repetitions initiated by random guess. As expected, we obtain a different
587 set of optimal parameters for each contact time, dipolar coupling, and MAS frequency.

588 The optimized transfer efficiencies are summarized in Figure 14. Remarkably, we have not found any
589 significant differences in the performance of the linear ramp with respect to the tangential sweep.
590 Both sweep methods yield the same total transfer efficiency, although they use different sweep
591 parameters. An example of the best sweep shapes obtained for a dipolar coupling b_{IS}=10 kHz and an
592 MAS frequency of 50 kHz is presented in Figure 15. The tangential sweeps tend to have a larger sweep
593 amplitude Δ and a smaller offset values δ_M when compared to the linear ramp.

594 We observe that very long contact times are required to obtain high transfer efficiencies. For
595 calculations involving different dipolar coupling strengths b_{IS} the same range of the reduced time
596 parameter Tb_{IS} is used. In this way, longer mixing times T are maintained for smaller dipolar couplings
597 b_{IS}. Better performance is obtained for cases with higher dipolar couplings which correlates with the
598 width of Hartmann-Hahn conditions in CP matching profiles. On the other hand, the transfer efficiency
599 decreases at higher MAS frequencies due to increased volume selectivity. The most challenging are
600 small dipolar couplings, on the order of 1 kHz and ultrafast MAS (>100 kHz) which are typical for ^{15}N-
601 ^{13}C spin pairs in proteins studied by proton-detected MAS solid-state NMR experiments. To more
602 efficiently average proton dipolar interaction, MAS probe development aims at smaller diameter
603 rotors to achieve higher MAS rotation frequencies. Currently, 0.4 mm MAS probes are in development
604 that can reach MAS frequencies of up to 200 kHz. Our predictions suggest that only 20% of the sample
605 will contribute to the detected NMR signal after a 10 ms ^{15}N-^{13}C CP mixing step at a MAS frequency of
606 200 kHz, i.e. up to 80% of the signal is lost in a single magnetization transfer step. The efficiency
607 increases to ca. 40% when a 40 ms long mixing period is used, provided that there are no signal losses
608 due to relaxation. However, note that the sensitivity in a pulse sequence with multiple CP transfer
609 elements depends on all previous transfer steps. The first CP element pre-selects a volume that is
610 maintained or further restricted in subsequent transfer elements.

611
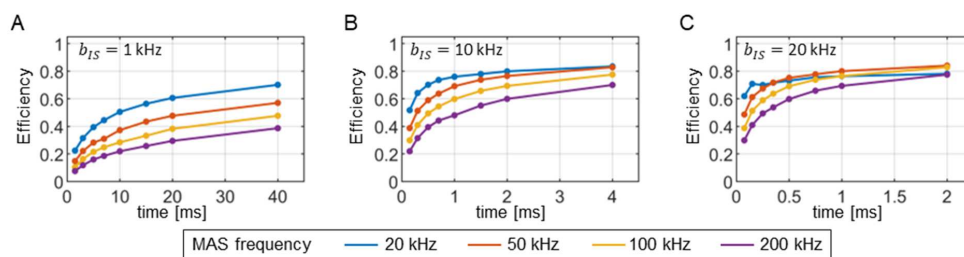
612

613 **Figure 14**. Maximum achievable transfer efficiencies in the cross-polarization experiment as a function
614 of contact time and MAS frequency using numerical optimizations. Similar efficiencies are obtained for
615 both the linear ramp and the tangential sweep, although different shape parameters have to be
616 employed. Dipolar couplings of 1 kHz, 10 kHz and 20 kHz are used in the simulations for panels A, B,
617 and C, respectively.

MAGNETIC
RESONANCE
Discussions
Open Access

618
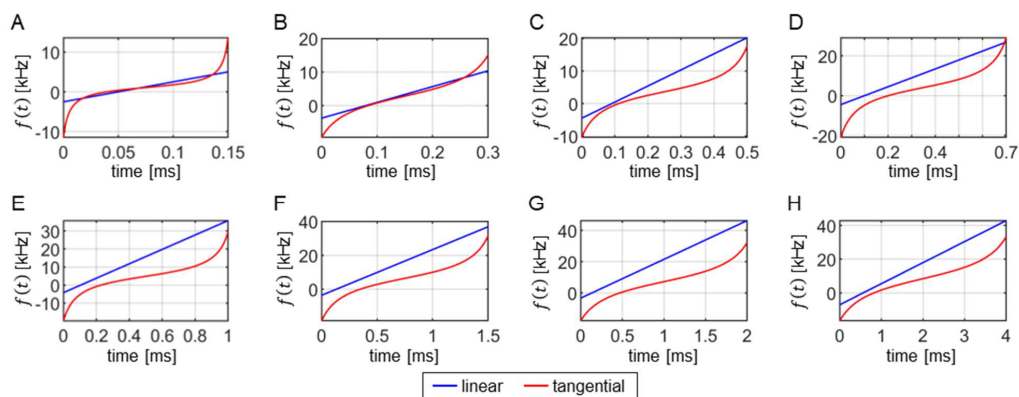
Figure 15: Comparison of optimal linear ramp (blue) and tangential sweep (red) shapes obtained by numerical optimizations at different contact times T=0.15, 0.3, 0.5, 0.7, 1.0, 1.5, 2.0, and 4.0 ms in panels A-H, respectively. For the optimization, a dipolar coupling b_{IS}=10 kHz was assumed. The calculations were performed assuming a MAS frequency of 50 kHz and a realistic RF inhomogeneity distribution. Although the two shapes are different, they yield virtually identical total transfer efficiencies.

We find that there is no difference between the linear ramp and the tangential shapes in terms of total transfer efficiency. In Figure 16, we compare these two methods (together with a constant amplitude CP) with respect to the width of the CP matching profile (panel A), the magnetization transfer buildup (panel B), and the sample volume selectivity (panel C). As expected, the RF amplitude sweep significantly improves the width and the height of the matching profile. The most important difference is that the tangential sweep yields higher efficiency near the center of the coil and lower efficiency at edges of the coil. Use of RF pulses and other recoupling elements can potentially result in a preselection of a particular sample volume that cannot be utilized by the linear ramp for a further transfer. Therefore, transfer elements should be optimized within the framework of the whole pulse sequence to minimize a differential preselection of the sample volume during calibration experiments.

636
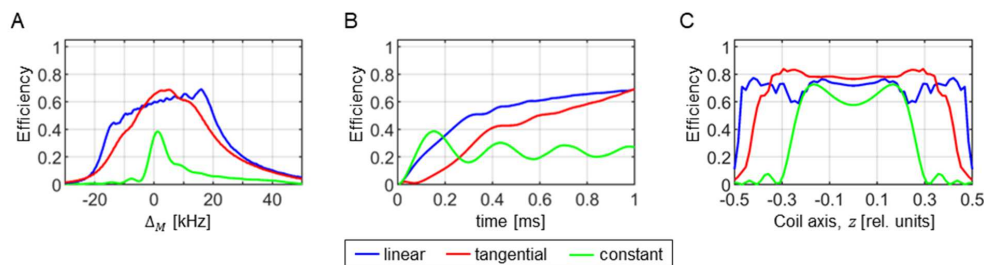
Figure 16: Comparison of the matching profiles (A), magnetization transfer buildups (B), and contribution to the transfer efficiency of individual volume elements along the coil axis (C) for an optimized linear ramp (blue), a tangential sweep (red), and a constant amplitude CP (green). For the optimization, a dipolar coupling b_{IS}=10 kHz was assumed. The calculations were performed assuming

MAGNETIC RESONANCE
Open Access
Discussions

641   a MAS frequency of 50 kHz and a realistic RF inhomogeneity distribution. The CP contact time was set
642   to T=1 ms. In (A) and (C), the constant amplitude CP was evaluated after 160 μs when it reaches
643   maximum transfer efficiency.

644

645   The linear ramp and the adiabatic tangential sweeps were calculated for the ZQ ($n = +1$) condition.
646   However, the shapes are equally applicable to any other $n = \pm 1$ Hartmann-Hahn condition, as the
647   corresponding effective Hamiltonian has the same form. The $n = \pm 2$ Hartmann-Hahn conditions
648   suffer from increased RF field inhomogeneity (factor of 2 in Eq. 40) and have different powder
649   averaging properties implied by the $g_2(\beta)$ term. Thus, a decreased CP transfer efficiency for the $n =$
650   ± 2 matching condition is expected.

651

652   The transfer efficiencies of all pulse sequences were verified using numerical simulations in SIMPSON.
653   To avoid overlap of the different Hartmann-Hahn matching conditions, the zero quantum ($n = +1$)
654   condition with $\omega_S^{NOM}/2\pi$ = 60 kHz was selected using MAS frequencies of 20 and 50 kHz, while the
655   double quantum ($n = +1$) condition with $\omega_S/2\pi$ = 30 kHz was used for a MAS frequency of 100 kHz.
656   The agreement between SIMPSON and the effective Hamiltonian calculations is excellent except for a
657   simulation in which a dipolar coupling of 20 kHz and a MAS frequency of 20 kHz was assumed. In this
658   case, the numerically evaluated transfer efficiencies are about 10% lower. A plausible explanation is
659   that the first order average Hamiltonian approximation does not provide the full description of the
660   spin dynamics when the dipolar coupling and the MAS frequency are of similar value (in other cases it
661   holds $b_{IS} \ll \omega_R/2\pi$).

662

663   ### 4. Conclusions

664   We have analyzed the magnetization transfer efficiency of the CP experiment as a function of the MAS
665   frequency in the presence of RF field inhomogeneity of a solenoid coil. We show that a sweep of the
666   RF amplitude through the Hartmann-Hahn matching conditions using either a linear ramp or a
667   tangential shape improves the performance in comparable way. We do not observe a difference in the
668   total transfer efficiency between these two methods. We find that magnetization transfer using a CP
669   recoupling element becomes inefficient in particular for small dipolar couplings for ultrafast MAS
670   experiments with rotation frequencies above 100 kHz. New recoupling methods that are designed
671   explicitly to account for inhomogeneous RF fields are needed to overcome this issue in the future.

672

673   **Author contribution**

674   ZT and BR conceived the project. AŠ carried out numerical calculations. JB, AŠ, BR and ZT discussed the
675   results, sketched the plot of the paper, and collaborated on the final text. ZT wrote the paper.

676   **Competing interests**

677   At least one of the (co-)authors is a member of the editorial board of Magnetic Resonance.

MAGNETIC RESONANCE
Open Access
Discussions

682 **References**

683 Aebischer, K., Tošner, Z., and Ernst, M.: Effects of radial radio-frequency field inhomogeneity on MAS
684 solid-state NMR experiments, Magnetic Resonance, 2, 523–543, https://doi.org/10.5194/mr-2-523-
685 2021, 2021.

686 ANDREW, E. R., BRADBURY, A., and EADES, R. G.: Nuclear Magnetic Resonance Spectra from a Crystal
687 rotated at High Speed, Nature, 182, 1659–1659, https://doi.org/10.1038/1821659a0, 1958.

688 Bak, M., Rasmussen, J. T., and Nielsen, N. C.: SIMPSON: A general simulation program for solid-state
689 NMR spectroscopy, J Magn Reson, 147, 296–330, https://doi.org/10.1006/jmre.2000.2179, 2000.

690 Baum, J., Tycko, R., and Pines, A.: Broadband and adiabatic inversion of a two-level system by phase-
691 modulated pulses, Phys Rev A (Coll Park), 32, 3435–3447,
692 https://doi.org/10.1103/PhysRevA.32.3435, 1985.

693 Brinkmann, A.: Introduction to average Hamiltonian theory. I. Basics, Concepts in Magnetic
694 Resonance Part A, 45A, e21414, https://doi.org/10.1002/cmr.a.21414, 2016.

695 Engelke, F.: Electromagnetic wave compression and radio frequency homogeneity in NMR solenoidal
696 coils: Computational approach, Concepts Magn Reson, 15, 129–155,
697 https://doi.org/10.1002/cmr.10029, 2002.

698 Gupta, R., Hou, G., Polenova, T., and Vega, A. J.: RF inhomogeneity and how it controls CPMAS, Solid
699 State Nucl Magn Reson, 72, 17–26, https://doi.org/10.1016/j.ssnmr.2015.09.005, 2015.

700 Hartmann, S. R. and Hahn, E. L.: Nuclear Double Resonance in the Rotating Frame, Physical Review,
701 128, 2042–2053, 1962.

702 Hediger, S., Meier, B. H., and Ernst, R. R.: ADIABATIC PASSAGE HARTMANN-HAHN CROSS-
703 POLARIZATION IN NMR UNDER MAGIC-ANGLE SAMPLE-SPINNING, Chem Phys Lett, 240, 449–456,
704 https://doi.org/10.1016/0009-2614(95)00505-x, 1995.

705 Hoult, D. I.: The principle of reciprocity in signal strength calculations - A mathematical guide,
706 Concepts Magn Reson, 12, 173–187, https://doi.org/10.1002/1099-0534(2000)12:4<173::aid-
707 cmr1>3.0.co;2-q, 2000.

708 Levitt, M. H.: Heteronuclear cross polarization in liquid-state nuclear magnetic resonance: Mismatch
709 compensation and relaxation behavior, J Chem Phys, 94, 30–38, https://doi.org/10.1063/1.460398,
710 1991.

711 Lowe, I. J.: Free Induction Decays of Rotating Solids, Phys Rev Lett, 2, 285–287,
712 https://doi.org/10.1103/PhysRevLett.2.285, 1959.

713 Marica, F. and Snider, R. F.: An analytical formulation of CPMAS, Solid State Nucl Magn Reson, 23,
714 28–49, https://doi.org/10.1016/S0926-2040(02)00013-9, 2003.

MAGNETIC RESONANCE
Open Access
Discussions

715   Metz, G., Wu, X. L., and Smith, S. O.: Ramped-amplitude cross-polarization in magic-angle-spinning
716   NMR, J Magn Reson A, 110, 219–227, https://doi.org/10.1006/jmra.1994.1208, 1994.

717   Paulson, E. K., Martin, R. W., and Zilm, K. W.: Cross polarization, radio frequency field homogeneity,
718   and circuit balancing in high field solid state NMR probes, J Magn Reson, 171, 314–323,
719   https://doi.org/10.1016/j.jmr.2004.09.009, 2004.

720   Peersen, O. B., Wu, X. L., and Smith, S. O.: Enhancement of CP-MAS Signals by Variable-Amplitude
721   Cross Polarization. Compensation for Inhomogeneous B1 Fields, J Magn Reson A, 106, 127–131,
722   https://doi.org/http://dx.doi.org/10.1006/jmra.1994.1014, 1994.

723   Pines, A., Gibby, M. G., and Waugh, J. S.: Proton-enhanced NMR of dilute spins in solids, J Chem Phys,
724   59, 569–590, https://doi.org/10.1063/1.1680061, 1973.

725   Ray, S., Ladizhansky, V., and Vega, S.: Simulation of CPMAS signals at high spinning speeds, J Magn
726   Reson, 135, 427–434, https://doi.org/10.1006/jmre.1998.1562, 1998.

727   Rovnyak, D.: Tutorial on analytic theory for cross-polarization in solid state NMR, Concepts in
728   Magnetic Resonance Part A, 32A, 254–276, https://doi.org/10.1002/cmr.a.20115, 2008.

729   Schaefer, J.: Schaefer, Jacob: A Brief History of the Combination of Cross Polarization and Magic
730   Angle Spinning, in: Encyclopedia of Magnetic Resonance, John Wiley & Sons, Ltd, Chichester, UK,
731   https://doi.org/10.1002/9780470034590.emrhp0161, 2007.

732   Stejskal, E. O., Schaefer, J., and Waugh, J. S.: Magic-angle spinning and polarization transfer in
733   proton-enhanced NMR, Journal of Magnetic Resonance (1969), 28, 105–112,
734   https://doi.org/10.1016/0022-2364(77)90260-8, 1977.

735   Tosner, Z., Andersen, R., Stevenss, B., Eden, M., Nielsen, N. C., Vosegaard, T., Stevensson, B., Eden,
736   M., Nielsen, N. C., and Vosegaard, T.: Computer-intensive simulation of solid-state NMR experiments
737   using SIMPSON, J Magn Reson, 246, 79–93, https://doi.org/10.1016/j.jmr.2014.07.002, 2014.

738   Tosner, Z., Purea, A., Struppe, J. O., Wegner, S., Engelke, F., Glaser, S. J., and Reif, B.: Radiofrequency
739   fields in MAS solid state NMR probes, JOURNAL OF MAGNETIC RESONANCE, 284, 20–32,
740   https://doi.org/10.1016/j.jmr.2017.09.002, 2017.

741   Wu, X. L. and Zilm, K. W.: Cross Polarization with High-Speed Magic-Angle Spinning, J Magn Reson A,
742   104, 154–165, https://doi.org/10.1006/jmra.1993.1203, 1993.

743